Subharmonic Entrainment Breather Solitons in Ultrafast Lasers

Tianhao Xian, Li Zhan,* Wenchao Wang, and Wenyan Zhang
State Key Laboratory of Advanced Optical Communication System and Networks, School of Physics and Astronomy, Shanghai Jiao Tong University, Shanghai 200240, China

(Received 27 May 2020; revised 3 August 2020; accepted 14 September 2020; published 12 October 2020)

We study theoretically and experimentally the subharmonic entrainment (SHE) breather soliton in mode-locked lasers for the first time, in which the ratio of the breather period to the round-trip time is an integer. We build a non-Hermitian degeneracy map of breather soliton, and illustrate that SHE arises between the two exceptional points (EPs). We obtain SHE at the ratio of 20, observe the evolution of breather soliton when tuning the gain and/or cavity loss, and prove that this phenomenon can improve the stability of breather soliton. Our research brings insight into the EP physics of ultrafast lasers and makes the mode-locked laser a powerful test bed for non-Hermitian degeneracy, which may open a new course in ultrafast laser research.

DOI: 10.1103/PhysRevLett.125.163901

Solitons, self-localized coherent structures, are ubiquitous in nature and have been observed in most branches of nonlinear science [1–5]. Mode-locked lasers constitute an ideal test bed for investigating solitons [6], where solitons arise from the balance among dispersion, nonlinearity, and environmental energy exchange. Once given the medium parameters, solitons generally display a fixed profile over propagation [7,8], which enables the application in designing pulse sources [9]. In many systems, the amplitude and duration of solitons can oscillate or breathe periodically. Breather solitons were first demonstrated in fiber cavities [10] and then observed in optical microresonators [11,12] and mode-locked lasers [13]. Because of strong connection with the Fermi-Pasta-Ulam recurrence [14], turbulence [15], modulation instability [16], and rogue wave formation [17], breather solitons have attracted considerable attention. Furthermore, the ability of breather soliton to increase the resolution of dual-comb source (composed of two frequency combs with slightly different repetition rates) implies that the breather soliton is attractive in practical applications [18].

Recently, the breather soliton generated in Kerr-nonlinear optical resonators was predicted to exhibit subharmonic entrainment (SHE): an integer ratio $T_b/T_r = n$ of the breather period T_b to the round-trip time T_r [19]. It is a special frequency locking that occurs between the two exceptional points (EPs) [20]. The EP is a branch point singularity in the parameter space [21–23] that arises when two or more eigenvalues of the non-Hermitian Hamiltonian and their corresponding eigenvectors become degenerate. Such degeneracies are distinct features of non-Hermitian systems, which do not obey conservation laws because the systems exchange energy with environment. The breather soliton laser, which has two frequencies (the repetition frequency f_r and the breather frequency f_b), can be deemed as a non-Hermitian system. The eigenvalues of the non-Hermitian Hamiltonian between the EPs are complex with the same real part [21], resulting in frequency locking in the breather soliton system, from which the SHE breather soliton arises. Although it was predicted in Kerr-nonlinear resonators [19], the SHE breather soliton has not been examined experimentally.

In this Letter, we present the first experimental observation of the SHE breather soliton. We find that the breather soliton laser exhibits non-Hermitian degeneracy in certain condition and that the SHE arises between the two EPs. Experimentally, we fabricate a mode-locked fiber laser, which is easily driven into the breather soliton regime by tuning the pump power and/or cavity loss. We record the change of breather soliton with the pump power and characterize SHE using dispersive Fourier-transform (DFT) technique [24–28] and dispersive temporal interferometer (DTI) [29]. We prove that SHE can enhance the stability of breather soliton. Simulations also prove that SHE arises between the EPs.

In principle, a stable mode-locked laser only sustains the modes at the free-running cavity frequency f_{r0} (corresponding to the cavity round-trip time T_{r0}) together with its harmonic (at the repetition frequency of mf_{r0}, m is an integer). Nevertheless, the breather soliton mode-locked laser somewhat is an unstable system, in which another mode, the free-running breather frequency f_{b0}, arises. Typically, $f_{b0} \ll f_{r0}$ [19]. Figure 1(a) depicts the free propagation of f_{b0}, which shows slight difference between nT_{r0} and the free-running breather period T_{b0} by $\Delta = T_{b0} - nT_{r0}$, with $|\Delta| \leq T_{r0}/2$. In Fig. 1(b), the soliton is treated as repeating in a period nT_{r0}, with uniformly distributed n solitons in each period. Each soliton repeats in the free-running subharmonic frequency $f_{nr0} = f_{r0}/n$.

 © 2020 American Physical Society

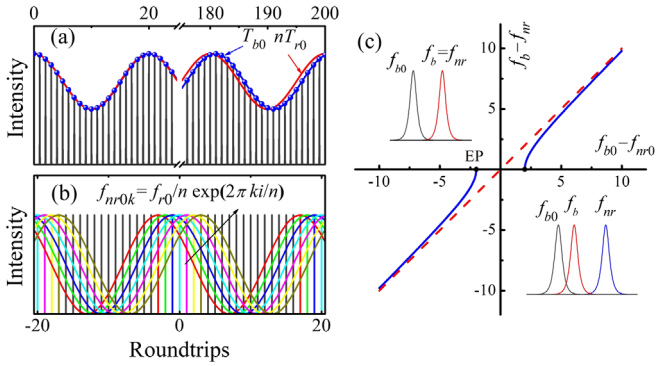

FIG. 1. Dynamics of non-Hermitian degeneracy in breather soliton laser. (a) Breather soliton train (the gray line). The blue dots are the breather amplitude at breather period T_b, and the period of the red line is nT_r. (b) Conceptual graph of the modes f_{nr0}. The adjacent modes have phase difference $2\pi/n$. The gray line is the soliton train. (c) The blue solid curve (red dashed line) shows the dependence of f_b on f_{b0} when $\kappa \neq 0$ ($\kappa = 0$) as per Eq. (2). The upper left (lower right) inset represents the dynamics of breather frequency shift between (out) the two EPs.

But, the location difference of these solitons makes the corresponding frequency components at f_{nr0} have different phases [Fig. 1(b)]; hence, the ensemble intensity at f_{nr0} is zero and undetectable. However, in the breather soliton laser, f_{b0} and f_{nr0} have close frequencies with difference $\delta = f_{b0} - f_{nr0}$ ($|\delta| \leq f_{b0}/2n$), and they can interplay over propagation, making the laser a non-Hermitian system (more detailed treatment is provided in Supplemental Material [30]).

In a laser that delivers stable breather soliton, the net gain for f_{b0} and f_{nr0} should be 0. Therefore, the interplay of the two frequencies can be described through a set of time-dependent coupled equations [20,21]:

$$\frac{d}{dt}\begin{pmatrix} a_1 \\ a_2 \end{pmatrix} = -2\pi i \begin{pmatrix} f_{nr0} & i\kappa \\ i\kappa & f_{b0} \end{pmatrix} \begin{pmatrix} a_1 \\ a_2 \end{pmatrix}, \tag{1}$$

where $a_{1,2}$ represent the amplitudes of f_{nr0} and f_{b0} components, and κ is the coupling rate. Here, the coupling between f_{nr0} and f_{b0} components may be induced by the round-trip change of gain, total nonlinearity, loss, or the environmental perturbation. Clearly, the laser displays a frequency locking-unlocking transition when varying f_{b0}, which can be manipulated by tuning cavity parameters like pump power and loss. Equation (1) has two eigenvalues, namely $(f_{nr0} + f_{b0})/2 \pm \sqrt{\delta^2/4 - \kappa^2}$, one of which is the breather frequency f_b while the other the subharmonic cavity frequency f_{nr}. We can see that $f_{nr} \approx f_{nr0}$ in the laser because most of the energy is locked into f_{nr0} and its harmonic. Thus, we obtain the expression of f_b [21,30]:

$$f_b = f_{nr} + \mathrm{sgn}(\delta)\sqrt{\delta^2 - 4\kappa^2}. \tag{2}$$

This equation has identical form with the one in Ref. [19]; here, we directly obtain such locking from the coupled equations. Equation (2) is plotted in Fig. 1(c). When $\delta = \pm 2\kappa$, an EP occurs, where the two eigenvalues coalesce (upper left inset). Near EPs ($|\delta| > 2\kappa$), the breather frequency is pulled by the soliton subharmonic frequency, as shown in the lower right insert in Fig. 1(c). Between the EPs, f_b is a complex number in Eq. (2), whose real part represents the breather frequency and is equal to f_{nr}. The SHE arises in this region. For simplicity, f_b henceforward represents the real part of Eq. (2).

To observe the dynamics of breather solitons, we fabricated a mode-locked laser, sketched in Fig. 2(a). The laser incorporates a 1.36 m Er-doped fiber (EDF), pumped by a 980 nm laser. The other fibers are the single-mode fibers (SMF), and the total cavity length is 4.82 m. The group velocity dispersion β_2 is 65 ps^2 km^{-1} for EDF and -22 ps^2 km^{-1} for SMF at 1550 nm. The laser is mode locked with the nonlinear polarization rotation (NPR) technique, which functions as an artificial saturable absorber through a polarization dependent isolator (PDI) and two polarization controllers (PCs) [31]. The pulse spectra are single-shot monitored by the DFT technique through 10 km SMF and the relative time and phase of adjacent pulses are measured by the DTI [30]. The DFT technique can stretch the pulse to map its spectrum into a temporal waveform [24]. The DTI is a novel technique for ultrashort time event measurement. As shown in Fig. 2(a), two optical couplers (OCs) and the extra fibers (EFs) reassemble the solitons from adjacent round-trips into a closely spaced dual-soliton pulse with time separation τ. The pulse is then stretched by 10 km SMF into a time interferogram with interference fringes. Then, the relative separation and phase of the two solitons are encoded into

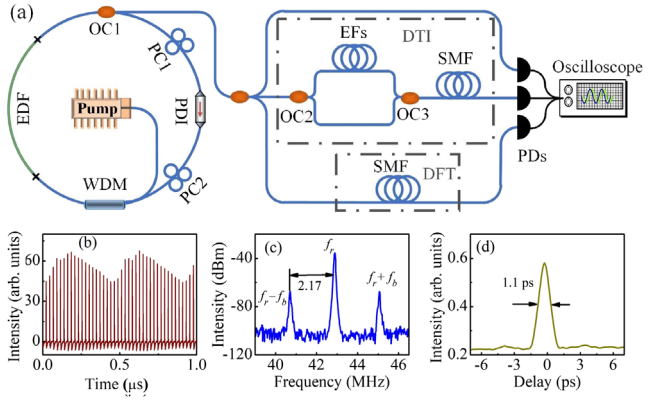

FIG. 2. Breather soliton laser. (a) The experimental setup. The left part is the mode-locked fiber laser and the right part is the real-time detection system. (b)–(d) Pulse train, frequency spectrum, autocorrelation trace of the generated pulses when the pump power is 404 mW. (d) is the autocorrelation of time-averaged profile of the breather soliton because the profile oscillates at the breather frequency. OC, optical coupler; WDM, wavelength division multiplexer; EFs, extra fibers; PDs, photodetectors, 40 GHz; OC1, 50:50; OC2, 50:50; OC3, 35:65.

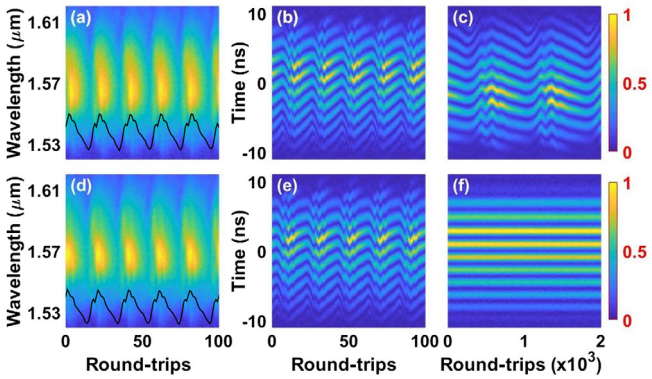

FIG. 3. Observation of breather solitons when the pump power is 404 mW (a)–(c) and 414 mW (d)–(f). (a),(d) DFT recording single-shot spectra over 100 consecutive round-trips. The black lines are the corresponding pulse intensity. (b),(e) Interferograms of adjacent pulses. (c),(f) Interferograms picked from (b),(e) with interval of 20 round-trips.

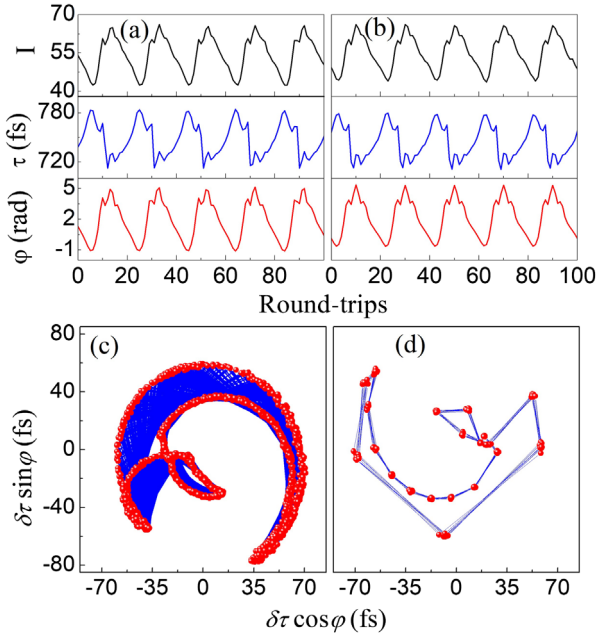

FIG. 4. Retrieved parameters of breather soliton. (a),(b) Evolution of breather soliton when the pump power is 404 mW (a) and 414 mW (b). The upper curves are the pulse energy evolution, the middle and the lower curves are the time separation and relative phase retrieved from interferograms respectively. (c), (d) Relation of retrieved time separation and relative phase in (a), (b) over 3000 consecutive round-trips. The radius and angle represent τ and φ.$\delta\tau = \tau - \tau_0$ represents the change of τ (τ_0 is a reference).

the interferogram. The total dispersion of the EFs is less than 0.5 fs/nm and $\tau < 0.8$ ps.

The laser works at 1570 nm with a repetition frequency of 42.8 MHz [Fig. 2(c)]. The onset of the breather soliton can be implemented through tuning the gain (pump power) and/or cavity loss (PCs) [13,32]. Here, we present the results of tuning the pump power to control the breather soliton. Breather soliton with time-averaged autocorrelation width of 1.1 ps is obtained when pump power is in the range of 400–430 mW [Fig. 2(d)].

Figure 3 illustrates the observation of breather solitons when the pump power is 404 and 414 mW. Figures 3(a) and 3(d) show that the respective spectrum compresses and stretches synchronously with the pulse energy change (black line) at a period of ~20 round-trips, which is a distinct feature of breather solitons. The interferogram evolutions of the breather soliton are illustrated in Figs. 3(b) and 3(e): the interference fringes change with the pulse energy synchronously. Then we extracted the continuous $20m$ round-trip from Figs. 3(b) and 3(e), shown in Figs. 3(c) and 3(f). Figure 3(c) exhibits similar periodic evolution as Fig. 3(b) at a frequency of $|f_b - f_r/20|$. By contrast, Fig. 3(f) shows identical fringe locations, which means $f_b = f_r/20$, i.e., the breather period is exactly 20 round-trips.

To probe whether all the pulses in a breather period are locked, we retrieved the time separation τ and relative phase φ of the adjacent solitons by the DTI. As displayed in Figs. 4(a) and 4(b), both τ and φ breathe with the intensity synchronously, proving the rationality to characterize SHE. Imitating the bound-state configuration in Refs. [28,33], we assign τ to the radius and φ to the angle to establish the polar diagram of breather solitons [Figs. 4(c) and 4(d)]. The points in Fig. 4(d) are locked into 20 discrete positions but no such order exists in Fig. 4(c). This clearly proves that all the pulses in the breather are locked when the pump power is 414 mW. Hence, the SHE with $T_b = 20T_r$ arises. The shape difference between Figs. 4(c) and 4(d) is because of the phase difference from the random jitter of round-trip time ($\delta\varphi = 2\pi\delta T_r/T_o$, T_o is the optical cycle). Moreover, changing the intracavity parameters by tuning the pump power and/or PCs, we have also obtained SHE of 16 and 18 round-trips, which is shown in Supplemental Material [30], Fig. S3.

The evolution of breather solitons was assessed in Fig. 5. Figure 5(a) exhibits that f_b decreases with the pump power, in which the plateau represents SHE at $T_b = 20T_r$. The data outside the plateau displays nonlinear dependence of f_{b0} on the pump power, similar to the relation between f_{b0} and F^2 in Ref. [19]. The plateau in Fig. 5(a) proves that the frequency locking of Eq. (2) arises in the breather soliton laser. Based on this, it can be deduced that the edges of the plateau are the EPs, where the non-Hermitian degeneracy occurs. Additionally, we calculated the frequency spectra of the breather soliton over 86 000 round-trips at the five red points in Fig. 5(a), as shown in Fig. 5(d). Compared with the other spectra, the spectrum at the plateau is smoother and has much smaller noise. All the spectra, other than that of the plateau, have small peaks at ±5.5 kHz, which may originate from environmental perturbation or gain jitter. The breather soliton at the plateau (SHE) is more stable than the ones out the plateau. Theoretically, the noise in f_b

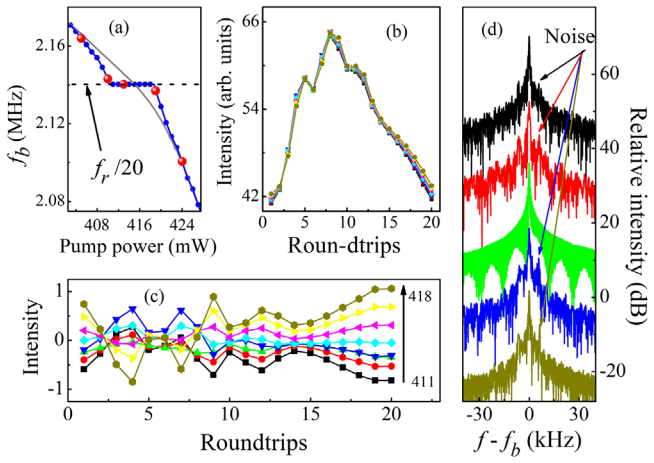

FIG. 5. Evolution of breather solitons. (a) f_b vs the pump power. The blue points are the detected frequency, and the gray curve represents the approximations of f_{b0}. The five red points are picked to calculate the breather frequency spectrum. (b) The breather profiles at different pump power in the plateau of (a). Each profile is averaged over 4300 period. (c) The relative change of different round-trips in (b). (d) Frequency spectra near the breather frequency. The five spectra correspond to the five red points in (a), and the pump power increases from bottom to top. The y axis is in arbitrary unit and the offset is 15 dB.

can be denoted as $\sigma_b = \sigma_{b0}|\delta|/\sqrt{\delta^2 - 4\kappa^2}$ (Supplemental Material [30], Eq. S3), where σ_{b0} is the noise in f_{b0}, induced by the jitter of intracavity parameters like gain and round-trip time. Hence, at the plateau, $\sigma_b \ll \sigma_{b0}$; if f_{b0} is far from the EPs, $\sigma_b = \sigma_{b0}$; near the EPs ($|\delta| > 2\kappa$), the noise increases when f_{b0} approaches the EPs (Fig. S1). Because the noise from intracavity parameters can only transmit to f_{b0} but can hardly affect to f_b in SHE, the stability of the breather soliton is significantly enhanced. The spectrum at the plateau has the narrowest linewidth in Fig. 5(d), which is evidence of its stability. Therefore, the SHE between the EPs can remarkably improve the performance of the breather soliton, which extends its application in many areas like the dual-comb source [18]. Moreover, it is feasible to magnify the noise of a laser using the EPs theoretically [30], which provides a new way to characterize the stability of a laser.

In addition, the breather profiles at the eight plateau dots are presented in Fig. 5(b), which shows similar breather profiles. By subtracting the average profile, we obtain Fig. 5(c), which elaborates the variation of breather profiles at each round-trip. The largest variation occurs at round-trip 20, but is still less than 5% of the pulse intensity. With increasing pump power, the pulse energy in the falling edge increases monotonically, but in the rising edge it does not: from the third to the eighth round-trips, the pulse energy initially increases, and then decreases with pump power. Thus, the energy has been reassigned, which introduces a slight change to the breather profile. This may result from the variation in the imaginary part of f_b.

To further interpret the SHE, we developed a piecewise numerical propagation model. The propagation in fibers follows the coupled nonlinear Schrödinger equations [34]:

$$\frac{\partial u_{1,2}}{\partial z} = \left[\left(-i\frac{\beta_2}{2} + \frac{g}{2\Omega_g^2}\right)\frac{\partial^2}{\partial t^2} + i\gamma\left|u_{1,2}\right|^2 + \frac{2i\gamma}{3}\left|u_{2,1}\right|^2 + \frac{g_n}{2}\right]u_{1,2}, \tag{3}$$

where $u_{1,2}$ are the envelopes of the pulses along the two orthogonal polarization axes of the fiber, γ is the nonlinearity coefficient, $g_n = g - \alpha$ is the net gain, and α is the loss. The gain $g = g_0 \exp(-E_s/2E_{\text{sat}})$ [35] for EDF and zero for SMF, where g_0 is the small signal gain, E_s is the pulse energy, and E_{sat} is the saturation energy. The gain bandwidth $\Omega_g = 50$ nm. The total transmission α_{NPR} of the NPR system can be expressed as [36]

$$\alpha_{\text{NPR}} = \begin{pmatrix} \cos\theta_1 \cos\theta_2 & \cos\theta_1 \sin\theta_2 \exp(i\theta_3) \\ \sin\theta_1 \cos\theta_2 & \sin\theta_1 \sin\theta_2 \exp(i\theta_3) \end{pmatrix}. \tag{4}$$

Here, $\theta_{1,2}$ are the angles between the transmission direction of PDI and fiber eigenaxis of out- and in-PDI, and θ_3 is the phase mismatching of two polarization directions. In our simulation, the transmission of OC $\alpha_{\text{OC}} = 0.4$, $\gamma = 2\ \text{W}^{-1}/\text{km}$, $\alpha = 0.2$ dB/km, $E_{\text{sat}} = 8$ nJ, $\theta_1 = 45$ deg, $g_0 = 2$, $\theta_3 = 4.5$ rad, the breather soliton is obtained in the range $64 \le \theta_2 \le 71$ deg, and its frequency is controlled by θ_2. We present the peak power evolution of the breather soliton over 3000 round-trips at $\theta_2 = 68.25$ deg [Fig. 6(a)] and 68.35 deg [Fig. 6(b)].

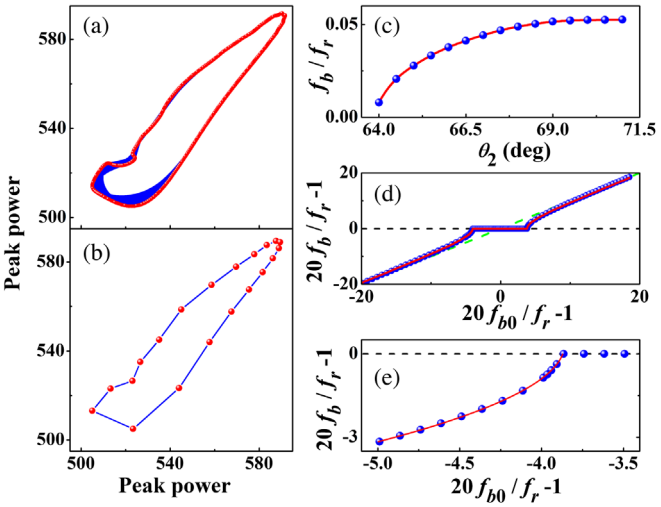

FIG. 6. Simulation of SHE breather soliton. (a),(b) Peak power evolution over 3000 round-trips in the free-running (a) and SHE (b) cases. $x(y)$ axis represents the peak power at the m $(m+1)$ round-trip. (c) Breather frequency f_b vs θ_2. (d) f_b vs f_{b0}. The blue dots are obtained from the simulations, and the red line is the fit using Eq. (2). (e) The close-up of (d) at the vicinity of the plateau. The red line is the parabolic fit of the blue dots.

In Fig. 6(b), the points are constrained in 20 discrete positions but the points in Fig. 6(a) are free to form a closed curve, which certifies the SHE when $\theta_2 = 68.35$ deg.

Figure 6(c) indicates that f_b monotonically increases with θ_2, which enables us to calculate f_{b0} near SHE. This is inaccessible in experiments because the breather soliton sustains much shorter range by tuning the pump power. The breather frequency evolution near $f_r/20$ is shown in Fig. 6(d), which fits well with Eq. (2) (the red line is the fitting). Figure 6(d) delivers similar SHE property as predicted in Ref. [19], but our simulation is achieved in mode-locked lasers. Furthermore, in Fig. 6(e) (the red line), near the EPs, the breather frequency approaches the EPs parabolically, which is a peculiar feature of the EPs.

Our simulations ascertain that the SHE behavior is a general phenomenon. The fittings in Figs. 6(d) and 6(e) highlight that the SHE breather soliton arises at the frequency locking between the two EPs. The noise from the gain or the environment can be transmitted to f_{b0}, which induces the instability of breather soliton. But because of the coupling, the SHE obstructs the noise transmission from f_{b0} to f_b; therefore, the SHE can stabilize the breather soliton. Reciprocally, the stability of f_b can help to distinguish whether the breather soliton is in SHE, which is also effective in Kerr-nonlinear microresonators. In this way, the repetition frequency that is too high (beyond 100 GHz) to be detected directly, can be measured through f_b by tuning the system into the SHE state (judged by noise).

In conclusion, we reported the first observation of SHE breather soliton in a mode-locked laser. This can help to measure the ultrahigh pulse-repetition rate that is electronically inaccessible [19]. Moreover, we have proved that the SHE behavior can enhance the stability of breather solitons, and provided a feasible way to improve the performance of dual-comb sources [18]. Furthermore, by building a non-Hermitian degeneracy model of breather soliton system, we introduced EP physics into the mode-locked lasers, which would attract research attention to such novel phenomena, and initiate a new course of ultrafast dynamic study. We believe this dynamical synchronization will have widely applications, especially in femtosecond pulse synthesis and frequency-comb generation.

This work was funded by the National Natural Science Foundation of China under Grant No. 11874040, and the Foundation for leading talents of Minhang, Shanghai.

*Corresponding author.
lizhan@sjtu.edu.cn

[1] J. Denschlag *et al.*, Science **287**, 97 (2000).
[2] E. Kuznetsov, A. Rubenchik, and V. E. Zakharov, Phys. Rep. **142**, 103 (1986).
[3] J. Nguyen, D. Luo, and R. G. Hulet, Science **356**, 422 (2017).
[4] L. F. Mollenauer, R. H. Stolen, and J. P. Gordon, Phys. Rev. Lett. **45**, 1095 (1980).
[5] G. I. Stegeman and M. Segev, Science **286**, 1518 (1999).
[6] D. Churkin, S. Sugavanam, N. Tarasov, S. Khorev, S. V. Smirnov, S. M. Kobtsev, and S. K. Turitsyn, Nat. Commun. **6**, 7004 (2015).
[7] P. Grelu and N. Akhmediev, Nat. Photonics **6**, 84 (2012).
[8] P. Ryczkowski, M. Närhi, C. Billet, J.-M. Merolla, G. Genty, and J. M. Dudley, Nat. Photonics **12**, 221 (2018).
[9] U. Keller, Nature (London) **424**, 831 (2003).
[10] F. Leo, L. Gelens, P. Emplit, M. Haelterman, and S. Coen, Opt. Express **21**, 9180 (2013).
[11] M. Yu, J. K. Jang, Y. Okawachi, A. G. Griffith, K. Luke, S. A. Miller, X. Ji, M. Lipson, and A. L. Gaeta, Nat. Commun. **8**, 14569 (2017).
[12] E. Lucas, M. Karpov, H. Guo, M. L. Gorodetsky, and T. J. Kippenberg, Nat. Commun. **8**, 736 (2017).
[13] J. Peng, S. Boscolo, Z. Zhao, and H. Zeng, Sci. Adv. **5**, eaax1110 (2019).
[14] C. Bao, J. A. Jaramillo-Villegas, Y. Xuan, D. E. Leaird, M. Qi, and A. M. Weiner, Phys. Rev. Lett. **117**, 163901 (2016).
[15] J. M. Soto-Crespo, N. Devine, and N. Akhmediev, Phys. Rev. Lett. **116**, 103901 (2016).
[16] M. Närhi, B. Wetzel, C. Billet, S. Toenger, T. Sylvestre, J.-M. Merolla, R. Morandotti, F. Dias, G. Genty, and J. M. Dudley, Nat. Commun. **7**, 13675 (2016).
[17] D. R. Solli, C. Ropers, P. Koonath, and B. Jalali, Nature (London) **450**, 1054 (2007).
[18] P. Liao *et al.*, in *Conference on Lasers and Electro-Optics, San Jose, 2018*, OSA Technical Digest (Optical Society of America, San Jose, 2018), paper JTh5A.4.
[19] D. C. Cole and S. B. Papp, Phys. Rev. Lett. **123**, 173904 (2019).
[20] M. Miri and A. Alù, Science **363**, eaar7709 (2019).
[21] Y. Lai, Y. Lu, M. Suh, Z. Yuan, and K. Vahala, Nature (London) **576**, 65 (2019).
[22] W. D. Heiss, J. Phys. A **37**, 2455 (2004).
[23] S. Özdemir, S. Rotter, F. Nori, and L. Yang, Nat. Mater. **18**, 783 (2019).
[24] K. Goda and B. Jalali, Nat. Photonics **7**, 102 (2013).
[25] A. Mahjoubfar, D. V. Churkin, S. Barland, N. Broderick, S. K. Turitsyn, and B. Jalali, Nat. Photonics **11**, 341 (2017).
[26] G. Herink, F. Kurtz, B. Jalali, D. R. Solli, and C. Ropers, Science **356**, 50 (2017).
[27] K. Krupa, K. Nithyanandan, U. Andral, P. Tchofo-Dinda, and P. Grelu, Phys. Rev. Lett. **118**, 243901 (2017).
[28] G. Herink, B. Jalali, C. Ropers, and D. R. Solli, Nat. Photonics **10**, 321 (2016).
[29] T. Xian, L. Zhan, W. Zhang, W. Zhang, and L. Gao, in *Optical Fiber Communication Conference, San Diego, 2020*, OSA Technical Digest (Optical Society of America, San Diego, 2020), paper M1C.4.
[30] See Supplemental Material at http://link.aps.org/supplemental/10.1103/PhysRevLett.125.163901 for more detailed discussions.
[31] A. Komarov, H. Leblond, and F. Sanchez, Phys. Rev. A **72**, 063811 (2005).
[32] Y. Du, Z. Xu, and X. Shu, Opt. Lett. **43**, 3602 (2018).

[33] Z. Q. Wang, K. Nithyanandan, A. Coillet, P. Tchofo-Dinda, and P. Grelu, Nat. Commun. **10**, 830 (2019).
[34] G. P. Agrawal, *Nonlinear Fiber Optics* (Academic, Boston, 2007).
[35] A. M. Weiner, *Ultrafast Optics* (Wiley, New Jersey, 2009).
[36] X. Feng, H. Tam, and P. K. A. Wai, Opt. Express **14**, 8205 (2006).